LETTER





Vibrational two-photon microscopy for tissue imaging: Short-wave infrared surface-enhanced resonance hyper-Raman scattering

Jacob E. Olson¹ | Jung Ho Yu^{2*} | Rebekah L. Thimes¹ | Jon P. Camden^{1*}

*Correspondence

Jung Ho Yu, Department of Radiology, Molecular Imaging Program, Stanford University School of Medicine. Stanford, CA 94305, USA.

Email: junghyu@stanford.edu

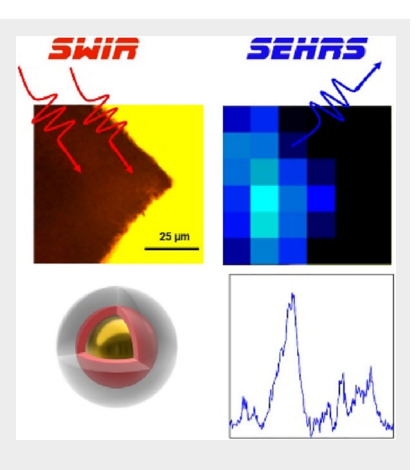
Jon P. Camden, Department of Chemistry and Biochemistry, University of Notre Dame, Notre Dame, IN 46556, USA. Email: jon.camden@nd.edu

Funding information

Department of Radiology at Stanford University School of Medicine; U.S. National Science Foundation, Grant/ Award Number: CHE-1709566; University of Notre Dame

Abstract

Multiphoton microscopy using short-wave infrared (SWIR) radiation offers nondestructive and high-resolution imaging through tissue. Two-photon fluorescence (TPF), for example, is commonly employed to increase the penetration depth and spatial resolution of SWIR imaging, but the broad spectral peaks limit its multiplexing capabilities. Hyper-Raman scattering, the vibrational analog of TPF, yields spectral features on the order of 20 cm⁻¹ and



reporter-functionalized noble metal nanoparticles (NPs) provide a platform for both hyper-Raman signal enhancement and selective targeting in biological media. Herein we report the first tissue imaging study employing surface-enhanced resonance hyper-Raman scattering (SERHRS), the two-photon analog of surface-enhanced resonance Raman scattering. Specifically, we employ multi-core gold-silica NPs (Au@SiO2 NPs) functionalized with a near infrared-resonant cyanine dye, 3,3'-diethylthiatricarbocyanine iodide as a SERHRS reporter. SWIR SERHRS spectra are efficiently acquired from mouse spleen tissue. SWIR SERHRS combines two-photon imaging advantages with narrow vibrational peak widths, presenting future applications of multitargeted bioimaging.

KEYWORDS

short-wave infrared (SWIR), surface-enhanced Raman scattering (SERS), surface-enhanced hyper Raman scattering (SEHRS), surface-enhanced resonance hyper-Raman scattering (SERHRS)

INTRODUCTION

Optical imaging is a nondestructive technique for interrogating the local environment and observing biological processes in tissue. Performing optical measurements in vivo requires passing light through the tissue barrier with

minimal losses from absorption and scattering. The penetration depth of visible and nearinfrared (NIR) light (~700 nm–1 $\mu m)$ is limited by absorption losses due to melanin and hemoglobin [1]. Short-wave infrared (SWIR) (~1–2 $\mu m)$ excitation, however, mitigates these losses, thereby increasing the available penetration depth through

¹Department of Chemistry and Biochemistry, University of Notre Dame, Notre Dame, Indiana, USA

²Department of Radiology, Molecular Imaging Program at Stanford, Stanford University School of Medicine, Stanford, California, USA

tissue [2]. For example, 1450 nm radiation reaches tissue penetration depths up to 100 μm , which is about twice that obtained using 1000 nm radiation [3]. Developments in SWIR imaging now enable through-skull in vivo brain imaging [4]. One-photon SWIR imaging microscopies, however, are limited in their resolution due to delocalized excitation volume. Although confocal setups can increase resolution, it comes at the cost of decreased collection efficiency and longer acquisition times [5].

Multiphoton microscopy has excitation volumes that are natively confined to the focal point, affording higher imaging resolution and higher image contrast than one-photon methods [6]. SWIR lasers are well suited for multiphoton methods because detection of the upconverted photons is achieved with highly efficient, low dark count Si detectors [7]. The combination of deeply penetrating SWIR radiation and high-resolution imaging has permitted in vivo analysis of biological processes on micron scales [8, 9]. Multiphoton processes, however, are inherently weak, often requiring designer reporters [10].

Noble metal nanoparticles (NPs) are a versatile substrate for enhancing signals via localized surface-plasmon resonances. NP-based methods such as surface-enhanced fluorescence [11] and surface-enhanced Raman scattering (SERS) [12, 13] leverage plasmonic NPs for signal enhancement. For passivation in biological media, NPs can be coated with a silica shell and subsequently functionalized with bioactive species, such as aptamers, for selective localization in tissue [14, 15]. Extension of the NP-based methods to two-photon processes has seen use in two-photon luminescence from NPs [16, 17] and twophoton fluorescence (TPF) [18] for high-resolution bioimaging. Unfortunately, the multiplexing capabilities of SWIR fluorescence and luminescence are limited by their broad spectral bandwidth [19]. Although the uniformsized quantum dots provide highly spectrally resolved TPF, their reported full width at half maximum (FWHM) at the NIR wavelength is 1300 cm^{-1} [20], which is still far larger than the FWHM of our SEHRS nanoparticles (100 cm⁻¹). Vibrational spectroscopies, however, have the ability to multiplex greater than 10 tags [21].

Surface-enhanced hyper-Raman scattering (SEHRS), the two-photon analog of SERS, is a NP-based two-photon method which measures a vibrational fingerprint [22, 23]. Hyper-Raman scattering is a type of nonlinear light scattering resulting in photons at $\nu_{\rm HRS} = 2\nu_{\rm i} - \nu_{\rm vib}$, where $\nu_{\rm i}$ is the incident radiation and $\nu_{\rm vib}$ is a molecular vibration. Hyper-Raman scattering is an inherently weak process, but analyte adsorption on a plasmonic NP overcomes this weak signal by supplying large signal enhancements, up to ~10^{12}, for aggregated NPs [24]. Similar to SERS, the narrow bandwidth of SEHRS and availability of multiple commercially available reporters allow for clear distinction of spectroscopic signatures when multiplexing [25].

Although most previous SEHRS studies have focused on the fundamental scattering process [26–31], SEHRS has proven to be a sensitive analytical method for trace detection [25, 32]. While SEHRS imaging has been explored, previous studies are limited to sensing in cellular environments with NIR excitation, and NP aggregates without physiologically stable protective layers [25, 33]. Recent work shows that 1550 nm SEHRS yields high-quality SWIR SEHRS spectra [34, 35] and the commercially available NIR SERS tag 3,3′-diethyl-thiatricarbocyanine iodide (DTTC) produces higher signal than rhodamine 6G [34]. In parallel, the synthesis of gold-silica shell NPs have been well established for syntheses and biocompatibility in mice [36, 37].

Herein, we present the first tissue-imaging application of SWIR surface-enhanced resonance hyper-Raman scattering (SERHRS) by accumulating SERHRS-active and physiologically stable silica-coated gold NPs in a murine spleen. DTTC-coded multicore Au NPs (DTTC Au@SiO₂ NPs) consist of a gold core, DTTC, and outer silica shell. The DTTC Au@SiO₂ NPs are injected into a mouse where they localize in the spleen, which is then removed for analysis. The SWIR SERHRS response of the DTTC Au@SiO₂ NPs in the spleen is then spatially mapped. We further explore the SERHRS response throughout the tissue sample compared to surface-enhanced resonant Raman scattering (SERRS) to show SERHRS is a viable imaging technique in tissue.

EXPERIMENTAL

Synthesis of gold core-DTTC-silica shell nanoparticles (DTTC Au@SiO₂ NPs)

The DTTC $Au@SiO_2$ NPs were synthesized by the simultaneous addition of 3,3-diethylthiatricarbocyanine iodide (DTTC, Sigma-Aldrich) and tetraethyl orthosilicate (TEOS, 99.999%, Sigma-Aldrich) silica precursor to the 60 nm gold NPs colloidal solution, prepared by Turkevich method [38]. To 2 mL of 60 nm gold nanoparticle solution (2 nM), 300 μ L of 28% NH₄OH, 2 mL of water, and 30 mL of isopropyl alcohol were gently added while stirring at 500 rpm. Then, 1600 mL of TEOS and 10 mg of DTTC mixture in 9 mL of isopropyl alcohol was rapidly added to the NP solution and reacted for 30 minutes. The produced DTTC $Au@SiO_2$ NPs were purified by washing with ethanol and pelletized by centrifugation.

The NP surface was PEGylated to have physiological stability for administration into the mice. To 1 mL of 1 nM DTTC Au@SiO₂ NPs solution in ethanol, 150 mL of NH₄OH in ethanol (2 M, Sigma-Aldrich), 20 mL of TEOS, and 100 mL of (3-mercaptopropyl) trimethoxysilane (MPTMS, Sigma-Aldrich) were added. The solution was then reacted at 70°C for 2 hours to

functionalize the NP surface with thiol. Then, the thiolfunctionalized DTTC Au@SiO2 NPs were PEGylated by adding 100 mg of methoxy polyethylene glycol maleimide (molecular weight 5 kDa, Sigma-Aldrich) to 1 mL of 1 nM thiolated NP in 10 mM 3-(N-morpholino)propanesulfonic acid (MOPS) buffer solution (pH 7.4). The PEGylated DTTC Au@SiO₂ NPs were purified by washing with water and pelletizing through the centrifuge multiple times. The NPs were stored in 5% glucose in water solution at 4°C. Finally, the NPs were characterized using transmission electron microscopy (JEM 1400, JEOL, 120 kV with LaB₆ emitter) and the concentration and hydrodynamic size distribution of NPs were measured with Nanoparticle Tracking Analysis (NanoSight, Malvern). Figure 1B shows a size distribution of the DTTC Au@SiO₂ NPs, where >50% of the NPs exist as monomers with a mean diameter of 253 \pm 69 nm.

Synthesis of Lee and Meisel Au NPs

Citrate-capped Au NPs used for DTTC Au NPs samples were synthesized using the Lee and Meisel method [39]. Two hundred and forty-seven milligrams of HAuCl₄ was added to 500 mL of deionized water H₂O and brought to a boil. Then 540 mg of sodium citrate was dissolved in 25 mL of H₂O and added dropwise to the boiling solution. The resulting solution was stirred until it turned a deep wine red color then was allowed to cool. The NPs were then diluted to 1 L with DI H₂O. Figure S2A shows UV-Vis characterization of the Au NPs gave a $\lambda_{max} = 522$ nm. Figure S2B displays STEM imaging of the Au NPs shows a mean diameter of 21 ± 5 nm. To serve as a reference for the DTTC Au@SiO₂ NPs, DTTC was added to the Au NP colloids, for a final DTTC concentration of 20 μ M, and vortexed for 30 minutes. The DTTC functionalized Au NPs were then aggregated using NaBr.

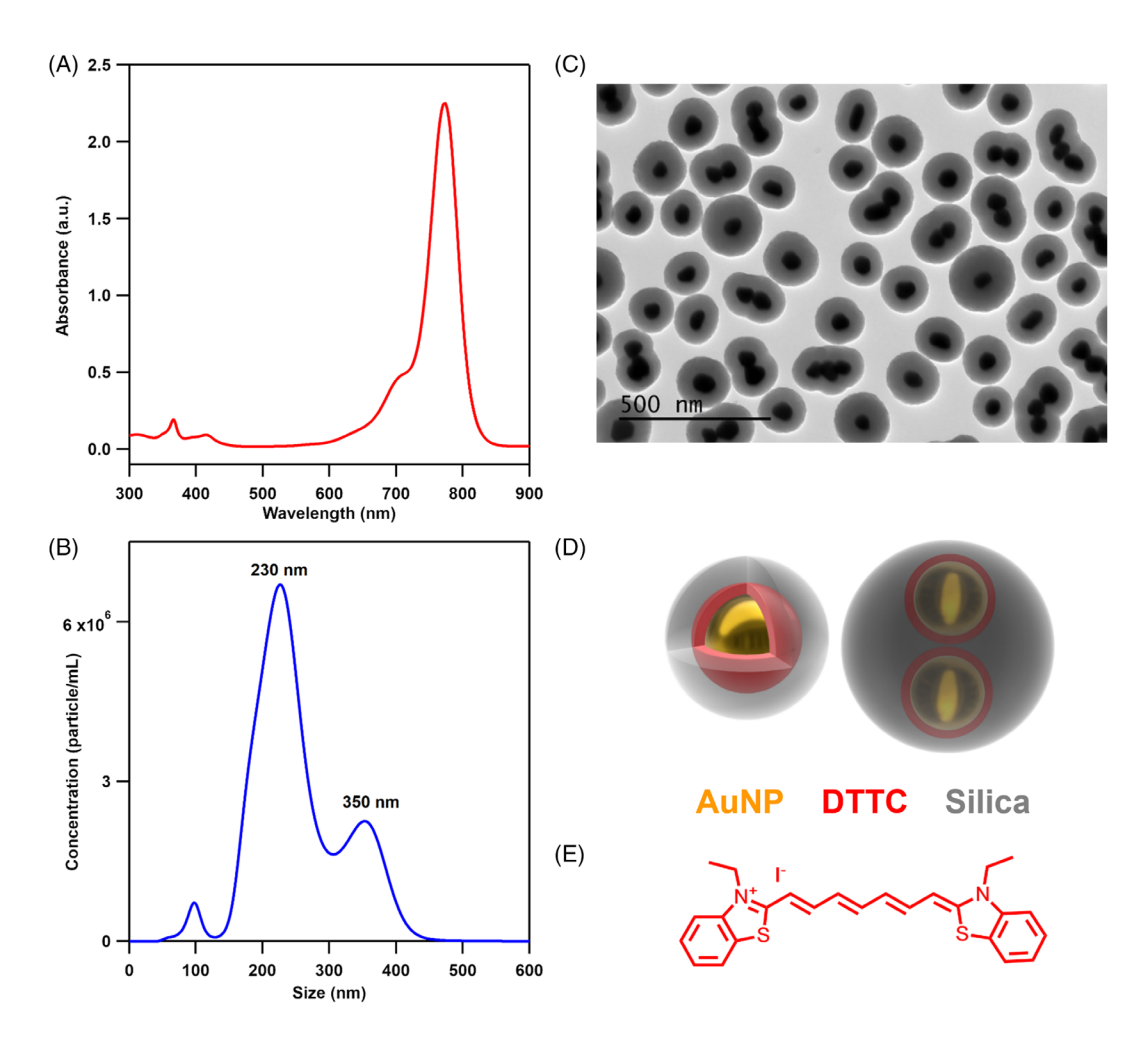


FIGURE 1 (A) UV-Vis absorption of $10 \,\mu\text{M}$ DTTC in dichloromethane. Max absorbance is at $\lambda = 772 \,\text{nm}$. (B) Size distribution of the DTTC Au@SiO₂ NPs where the 230 nm peak consists of monomeric DTTC Au@SiO₂ NPs and the 360 nm peak consists of oligomers. (C) Transmission electron microscope image of the DTTC Au@SiO₂ NPs nanoparticles displaying monomers and oligomers [31]. (D) Schematic of the DTTC Au@SiO₂ NPs monomer and oligomer where gold is the AuNP core, red is the DTTC layer and gray is the silica shell. (E) Molecular structure of the DTTC reporter dye. DTTC, 3,3'-diethyl-thiatricarbocyanine iodide; NPs, nanoparticles

Spleen preparation

Two hundred milliliters of 1 nM DTTC Au@SiO $_2$ NPs solution in 5% glucose was intravenously injected through the tail veins of the female 8-week-old nude mice (n = 3, Charles River Laboratories). Twenty-four hours after the injection, the spleen was excised and fixed with formalin for 2 days. All procedures performed on the animals were approved by the Institutional Animal Care and Use Committee at Stanford University (APLAC #14465) and were conducted within the NIH guidelines for the humane care of laboratory animals.

SERHRS and SERRS characterization

The SERHRS spectra were taken using an optical parametric oscillator (OPO) (APE picoEmerald), at 1550 nm laser wavelength. The OPO delivers 5 ps pulses at an 80 MHz repetition rate. The laser light was focused with an inverted microscope objective (Nikon Ti-U, \times 20, numerical aperture (NA) = 0.5) with 5 mW of average power at the objective. The laser spot size at the focus is approximated as the e^{-2} diameter as 10 µm, with average and peak irradiances of approximately 5 kW cm⁻² and 10 MW cm⁻², respectively. The backscattered radiation was collected through the same objective and passed through a Rayleigh rejection filter (Semrock) and dispersed with a spectrometer (Princeton Instruments Acton SP2300, 150 g mm⁻¹, blazed at 500 nm). The scattered photons were then detected with a back-illuminated, deep depletion Si charge-coupled device (CCD) detector (Excelon) and analyzed using Winspec32 software (Princeton Instruments). The SERHRS data were then analyzed in MATLAB (MathWorks) and plotted in IgorPro (WaveMetrics).

SERRS spectra were acquired with a 785 nm diode laser (Spectra Physics Newport). The light was focused with an inverted microscope objective (Nikon Ti-U, \times 20, NA = 0.5) with 1 mW of average power at the objective. The back-scattered radiation was collected through the same objective and passed through a Rayleigh rejection filter (Semrock) and dispersed with a spectrometer (Princeton Instruments Acton SP2300, 600 g mm⁻¹, BLZ = 500 nm). The Raman scattered photons were then detected with a back-illuminated, deep depletion Si CCD detector (Excelon) and analyzed using Winspec32 software (Princeton Instruments). The SERRS data were then analyzed in MATLAB (MathWorks) and plotted in IgorPro (WaveMetrics).

SERHRS and SERRS imaging

The DTTC Au@SiO₂ NP spleen sample was illuminated from the top via a halogen lamp and focused with a

condenser lens. Bright field images were acquired using a CMOS camera (Nikon DS-Ri2) and processed using NIS Elements D software (Nikon). The DTTC Au@SiO $_2$ NP spleen sample was translated with an XY stage (Prior ProscanIII) along a region of interest that constitutes a 120 μ m \times 120 μ m square. The 20 μ m step size was chosen to be larger than the approximated spot size to avoid overlap. The hyperspectral imaging analysis was performed using self-written code in MATLAB (MathWorks). The pixels in the hyperspectral images correspond to the peak areas of the most intense peak in the spectra, the 1070 cm $^{-1}$ peak and the 1131 cm $^{-1}$ peak, for SERHRS and SERRS, respectively. The peak areas are then normalized to the most intense peak area for the region of interest (ROI).

For the given SERHRS parameters, sample damage was not observed until the acquisition time was increased above 10 seconds per spot and the average power was increased above 10 kW cm⁻². For SERRS, no evidence of damage was seen at the powers and integration times employed. The TPF imaging of live biological media generally employs the same excitation power of 5 mW, but with a shorter pulse duration (100 fs) and a smaller laser spot size (10⁻⁹ cm²), which produces the mean power density of 5 MW cm⁻² and the peak power density of 600 GW cm⁻² [6]. Therefore, the SERHRS imaging in this work was performed at significantly lower power density than the TPF imaging condition of live biological media [40].

RESULTS AND DISCUSSION

Figure 1 overviews the DTTC Au@SiO₂ NPs used as the SERHRS signal source. Figure 1B,C shows the DTTC Au@SiO₂ NPs have a distribution of monomeric and oligomeric forms of the Au NP core, with >25% existing as multicore oligomers. The outer silica shell acts as a protective layer, preventing desorption of DTTC and biofouling of the NP [41]. Au@SiO2 NPs have been previously employed for NIR SERS imaging experiments for their high signal intensity and stability in biological media [37, 42]. Previous reports on the stability of metal-silica core-shell NPs suggest that the silica shell degrades slowly once the NPs enter the endosome of the cell via endocytosis [43]. However, timescale of the degradation (over several days) is sufficiently longer than the NP-uptake (less than a day) and imaging acquisition time (a few minutes). In addition, SERHRS imaging of the NP-uptaken spleen occurred over several months without significant deterioration of the signal intensity. The reporter, DTTC is a commercially available, NIRresonant dye previously used for SERS applications [44, 45]. The DTTC Au@SiO2 NPs have not had additional modifications for SERHRS.

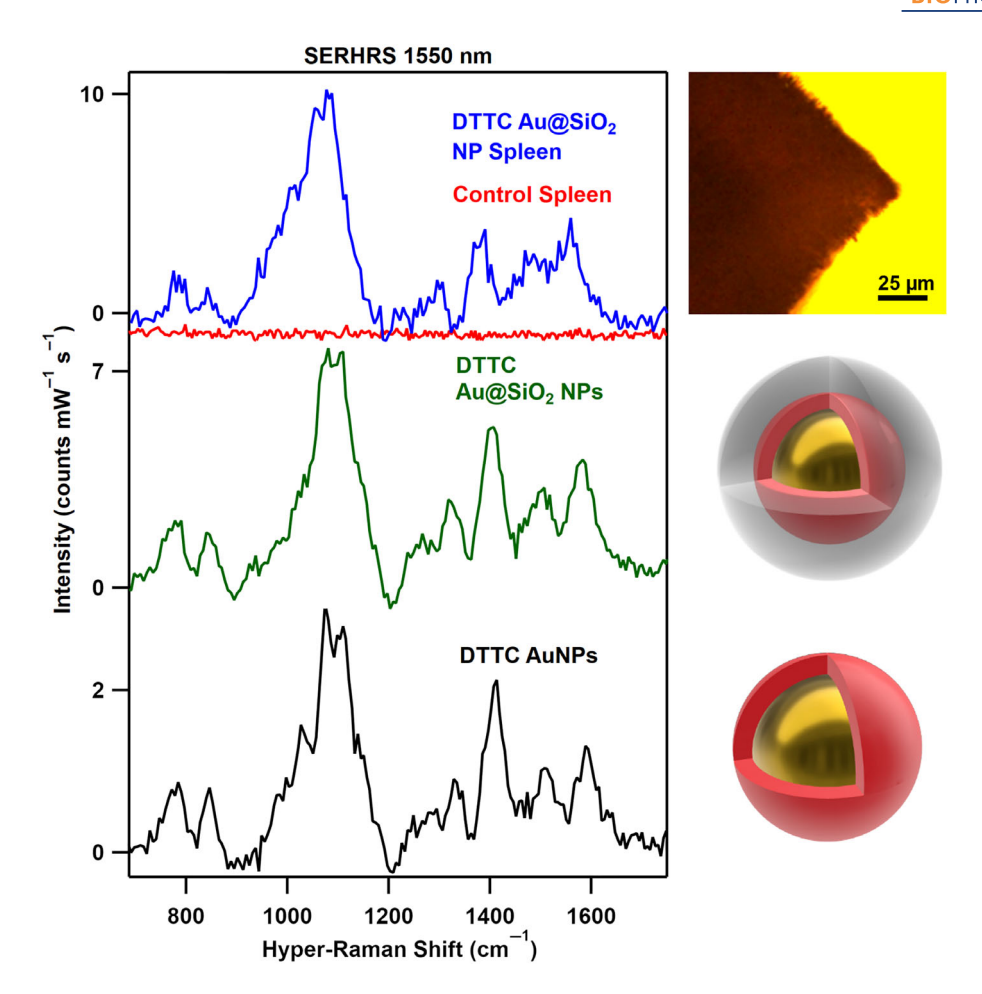


FIGURE 2 1550 nm SERHRS obtained from the DTTC Au@SiO₂ NP spleen (blue), the control spleen (red), the DTTC Au@SiO₂ NPs dropcast onto a glass slide (green), and Au NPs functionalized with DTTC (black). The DTTC Au@SiO₂ NPs maintain the DTTC SERHRS signature without a drop in SERHRS signal. When transferred to the spleen, the DTTC SERHRS signature persists and no drastic change in SERHRS signal is observed. DTTC, 3,3'-diethyl-thiatricarbocyanine iodide; NPs, nanoparticles; SERHRS, surface-enhanced resonance hyper-Raman scattering

An initial SERHRS test of the DTTC Au@SiO2 NPs was performed using the drop-cast method [15]. DTTC Au@SiO₂ NPs were dropped onto a glass slide forming a dense NP accumulation at the outer edge in a coffee-ring shape. Figure 2 shows that DTTC Au@SiO₂ NPs give a signature consistent with DTTC on Lee and Meisel Au NP aggregates [34]. The SERHRS signal is also slightly higher in the DTTC Au@SiO2 NPs, which could be due to the multicore NP oligomers supplying higher enhancement factor (EF)s or sampling of more NPs, as the coffeering method creates dense aggregates. Regardless, the DTTC Au@SiO2 NPs see no significant drop in performance from the typical dye on Au NP sample preparation. The use of NIR SERRS NPs presents a facile application to SWIR SERHRS methods without the need for sample optimization.

DTTC $Au@SiO_2$ NPs concentrated within a mouse spleen were used as the target for SWIR SERHRS imaging in tissue. The spleen is an ideal system for these NPs as

previous work has characterized that the accumulation of Au@SiO₂ NPs in mouse spleens induces no significant toxicity [36]. Previous studies indicate that ~20% of the administered gold-silica NPs are accumulated in the spleen [36]. Injection of 200 fmol of similarly structured NPs, it is expected that 40 fmol of the NPs will be accumulated in the spleen. Assuming a homogeneous distribution of particles and the average size of the spleen (70 mm³), we approximate the density of the NPs as 3.4×10^8 particle mm⁻³. Therefore, in the volume of the laser spot $(4 \times 10^{-6} \text{ mm}^3)$, we estimate approximately 1280 NPs are accumulated on average. Figure 2 shows that a control spleen, that is, without the introduction of NPs, yields no SERHRS signal, while the DTTC Au@SiO₂ NP spleen gives a SERHRS spectrum consistent with the signal from the DTTC Au@SiO2 NPs themselves. Further characterization of the DTTC Au@SiO2 NP spleen using 785 nm SERRS can be found in the Supporting Information.

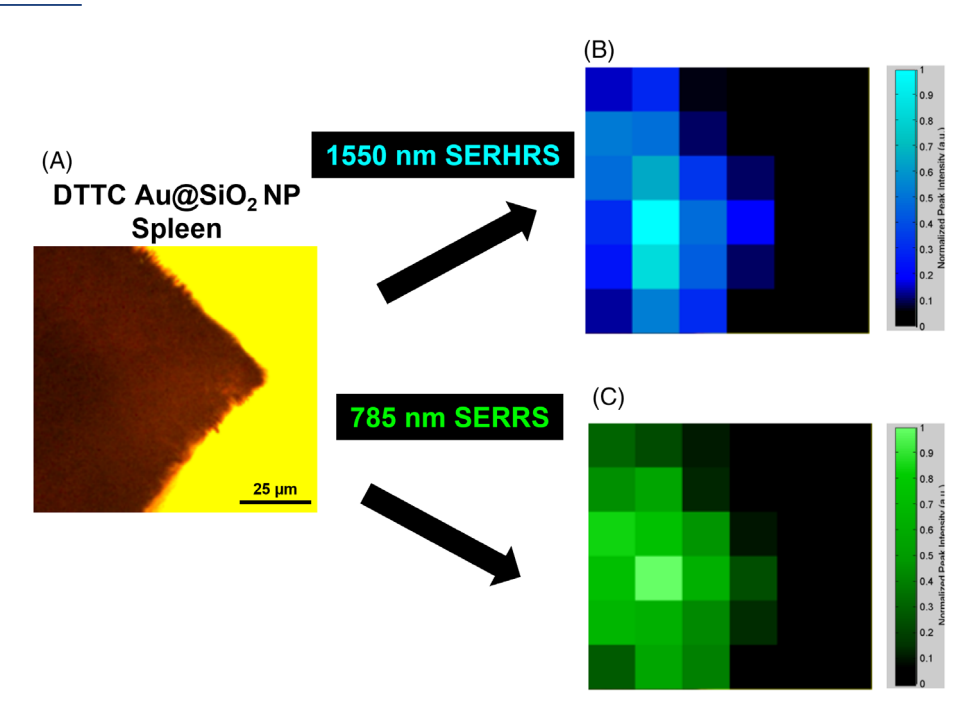


FIGURE 3 (A) A bright-field image of the DTTC $Au@SiO_2$ NP spleen sample placed on a glass slide. The corresponding hyperspectral images of the 1550 nm SERHRS (B) and 785 nm SERRS (C) for the bright-field image ROI. The color corresponds to the peak area of the most intense peak in the spectra, the 1070 cm⁻¹ peak and the 1131 cm⁻¹ peak, for SERHRS and SERRS, respectively. The ROI constitutes a 120 μ m × 120 μ m square where each step is 20 μ m. SERHRS spectra are acquired under conditions of 5 mW for 1 second. SERRS spectra are acquired in 1-second intervals at 1 mW incident power. DTTC, 3,3'-diethyl-thiatricarbocyanine iodide; NPs, nanoparticles; SERHRS, surface-enhanced resonance hyper-Raman scattering; SERRS, surface-enhanced resonant Raman scattering; ROI, region of interest

Figure 3 displays a bright-field image of the DTTC Au@SiO₂ NP spleen and its corresponding hyperspectral SERHRS and SERRS images. As a control, multiple SERHRS and SERRS spectra are taken off the DTTC Au@SiO₂ NP spleen, yielding no signal. The SERRS measurements of the same sample tissue provide a benchmark for evaluating SERHRS as a tissue imaging technique given its well characterized and widely studied applications [46]. Figure 3B,C shows hyperspectral SERHRS and SERRS images of the same ROI. A comparison of the SERHRS and SERRS normalized peak area values yields a correlation coefficient of 0.8. The similarity of signal distribution in SERHRS and SERRS indicates the capability of SERHRS to accurately measure the DTTC Au@SiO₂ NP localization in the spleen, and the fact that the SERHRS signal is localized to regions of strong SERRS activity further emphasizes the origin of the SERHRS signal is the DTTC Au@SiO₂ NPs. The nonlinear excitation dependence cannot compensate for the decreased spatial resolution when using long wavelength SWIR excitation; however, the resolution is not the primary motivation, rather it is the high penetration depth and reduced scattering for thick tissue imaging. For SERHRS collection, a high throughput 150 g mm⁻¹ detector was used to achieve efficient acquisition times of 1 second, while maintaining a sufficient resolution for

peak area analysis. This stands in contrast to previous SWIR SEHRS experiments on Ag NPs that have taken upward of 2 minutes for high signal-to-noise spectra [34]. SERHRS having an imaging speed similar to SERRS is promising for scaling to hyperspectral imaging of larger areas.

CONCLUSION

In this work, we present SWIR SERHRS as a vibrational two-photon technique for imaging in tissue. This method uses deeply penetrating SWIR radiation to spatially map the SERHRS response of DTTC Au@SiO₂ NPs in a mouse spleen. The highly efficient background-free SERHRS acquisition and use of established NIR SERRS NPs highlights the practicality of SWIR SERHRS as a tissue imaging technique. The ability to colocalize the SERHRS and SERRS response in the DTTC Au@SiO2 NP spleen with similar imaging speeds serves to validate SERHRS as a viable imaging method. While SERS imaging has advanced to rival the sensitivity of fluorescence, there has been almost no work devoted to the optimization of hyper-Raman chromophores or nanostructures for SEHRS. A significant improvement in the brightness of the SEHRS probes would be required to achieve a sensitivity similar to that of TPF. The DTTC $Au@SiO_2$ NPs are not specifically optimized for SEHRS, presenting future opportunities for optimization of NPs with multiple bright SEHRS tags for multiplexing applications [10]. In conjunction with functionalization of NPs with bioactive ligands, SEHRS could see future applications for multiplexable targeted biomarker sensing [21]. Further, as SWIR ultrafast fiber laser systems improve [47] and continuous-wave SEHRS configurations are optimized [48], SWIR SEHRS could see more cost-effective applications.

ACKNOWLEDGMENTS

This work was supported by the Early Cancer Detection Research Fund from the Department of Radiology, Division of Molecular Imaging Program at Stanford, Stanford University School of Medicine (Jung Ho Yu). This work was also supported by the University of Notre Dame and the U.S. National Science Foundation under Grant No. CHE-1709566 (Jacob E. Olson and Jon P. Camden).

CONFLICT OF INTEREST

The authors declare no financial or commercial conflicts of interest.

DATA AVAILABILITY STATEMENT

The data that support the findings of this study are available from the corresponding author upon reasonable request.

ORCID

Jacob E. Olson https://orcid.org/0000-0001-7110-1739 *Jung Ho Yu* https://orcid.org/0000-0003-4101-513X

REFERENCES

- G. Zonios, J. Bykowski, N. Kollias, J. Invest. Dermatol. 2001, 117, 1452.
- [2] S. Golovynskyi, I. Golovynska, L. I. Stepanova, O. I. Datsenko, L. Liu, J. Qu, T. Y. Ohulchanskyy, J. Biophotonics 2018, 11, e201800141.
- [3] J. A. Carr, M. Aellen, D. Franke, P. T. C. So, O. T. Bruns, M. G. Bawendi, Proc. Natl. Acad. Sci. U. S. A. 2018, 115, 9080.
- [4] Z. Xue, S. Zeng, J. Hao, Biomaterials 2018, 171, 153.
- [5] F. Helmchen, W. Denk, Nat. Methods 2005, 2, 932.
- [6] W. R. Zipfel, R. M. Williams, W. W. Webb, Nat. Biotechnol. 2003, 21, 1369.
- [7] R. H. Wilson, K. P. Nadeau, F. B. Jaworski, B. J. Tromberg, A. J. Durkin, J. Biomed. Opt. 2015, 20, 30901.
- [8] A. M. Packer, D. S. Peterka, J. J. Hirtz, R. Prakash, K. Deisseroth, R. Yuste, *Nat. Methods* 2012, 9, 1202.
- [9] M. S. Pochechuev, I. V. Fedotov, O. I. Ivashkina, M. A. Roshchina, K. V. Anokhin, A. M. Zheltikov, J. Biophotonics 2018, 11, e201600203.
- [10] L. Xu, J. Zhang, L. Yin, X. Long, W. Zhang, Q. Zhang, J. Mater. Chem. C 2020, 8, 6342.
- [11] S. Huang, C.-W. Lin, J. Qi, A. M. Iyer, Y. He, Y. Li, N. M. Bardhan, D. J. Irvine, P. T. Hammond, A. M. Belcher, Adv. Mater. 2021, 33, 2006057.

- [12] X. Gu, M. J. Trujillo, J. E. Olson, J. P. Camden, Annu. Rev. Anal. Chem. 2018, 11, 147.
- [13] C. Krafft, M. Schmitt, I. W. Schie, D. Cialla-May, C. Matthäus, T. Bocklitz, J. Popp, Angew. Chem. Int. Ed. 2017, 56, 4392.
- [14] I. Freitag, C. Matthäus, A. Csaki, J. H. Clement, D. Cialla-May, K. Weber, C. Krafft, J. Popp, J. Biomed. Opt. 2015, 20, 1.
- [15] M. Blanco-Formoso, A. Sousa-Castillo, X. Xiao, A. Mariño-Lopez, M. Turino, N. Pazos-Perez, V. Giannini, M. A. Correa-Duarte, R. A. Alvarez-Puebla, *Nanoscale* 2019, 11, 21872.
- [16] J.-L. Li, M. Gu, Biomaterials 2010, 31, 9492.
- [17] H. Wang, T. B. Huff, D. A. Zweifel, W. He, P. S. Low, A. Wei, J.-X. Cheng, Proc. Natl. Acad. Sci. U. S. A. 2005, 102, 15752.
- [18] M.-Q. Zhu, G.-F. Zhang, C. Li, M. P. Aldred, E. Chang, R. A. Drezek, A. D. Q. Li, J. Am. Chem. Soc. 2011, 133, 365.
- [19] S. Zhu, Q. Yang, A. L. Antaris, J. Yue, Z. Ma, H. Wang, W. Huang, H. Wan, J. Wang, S. Diao, Proc. Natl. Acad. Sci. U. S. A. 2017, 114, 962.
- [20] P. M. Allen, W. Liu, V. P. Chauhan, J. Lee, A. Y. Ting, D. Fukumura, R. K. Jain, M. G. Bawendi, J. Am. Chem. Soc. 2010, 132, 470.
- [21] C. L. Zavaleta, B. R. Smith, I. Walton, W. Doering, G. Davis, B. Shojaei, M. J. Natan, S. S. Gambhir, *Proc. Natl. Acad. Sci. U. S. A.* 2009, 106, 13511.
- [22] F. Madzharova, Z. Heiner, J. Kneipp, Chem. Soc. Rev. 2017, 2017, 3980.
- [23] A. M. Kelley, Annu. Rev. Phys. Chem. 2010, 61, 41.
- [24] J. T. Golab, J. R. Sprague, K. T. Carron, G. C. Schatz, R. P. Van Duyne, J. Chem. Phys. 1988, 88, 7942.
- [25] M. Guhlke, Z. Heiner, J. Kneipp, Phys. Chem. Chem. Phys. 2016, 18, 14228.
- [26] C. B. Milojevich, D. W. Silverstein, L. Jensen, J. P. Camden, J. Am. Chem. Soc. 2011, 133, 14590.
- [27] C. B. Milojevich, D. W. Silverstein, L. Jensen, J. P. Camden, J. Phys. Chem. C 2013, 117, 3046.
- [28] J. E. Olson, A. Tripp, M. K. Linder, Z. Hu, M. R. Detty, L. Jensen, J. P. Camden, *J. Phys. Chem. C* **2018**, *122*, 25051.
- [29] C. B. Milojevich, D. W. Silverstein, L. Jensen, J. P. Camden, ChemPhysChem 2011, 12, 101.
- [30] J. E. Olson, Z. Hu, M. D. Best, L. Jensen, J. P. Camden, J. Chem. Phys. 2021, 154, 034703.
- [31] H. K. Turley, Z. Hu, L. Jensen, J. P. Camden, J. Phys. Chem. Lett. 2017, 8, 1819.
- [32] M. J. Trujillo, J. P. Camden, ACS Omega 2018, 3, 6660.
- [33] Z. Heiner, M. Guhlke, V. Zivanovic, F. Madzharova, J. Kneipp, Nanoscale 2017, 9, 8024.
- [34] H. K. Turley, J. P. Camden, Chem. Commun. 2014, 50, 1472.
- [35] Z. Heiner, F. Madzharova, V. Živanović, J. Kneipp, J. Raman Spectrosc. 2021, 52, 394.
- [36] A. S. Thakor, R. Luong, R. Paulmurugan, F. I. Lin, P. Kempen, C. Zavaleta, P. Chu, T. F. Massoud, R. Sinclair, S. S. Gambhir, Sci. Transl. Med. 2011, 3, 79ra33.
- [37] J.-H. Yu, I. Steinberg, R. M. Davis, A. V. Malkovskiy, A. Zlitni, D. T. Chung, L. D. Curet, A. L. D'Souza, K. oh Jung, E. Chang, J. Campbell, H. Frostig, S.-M. Park, G. Pratx, S. S. Gambhir, *Chem-Rxiv* 2020. https://doi.org/10.26434/chemrxiv.13232246.v1.
- [38] B. Enustun, J. Turkevich, J. Am. Chem. Soc. 1963, 85, 3317.
- [39] P. C. Lee, D. Meisel, J. Phys. Chem. 1982, 86, 3391.
- [40] A. Hopt, E. Neher, *Biophys. J.* **2001**, *80*, 2029.
- [41] C. Hanske, M. N. Sanz-Ortiz, L. M. Liz-Marzán, Adv. Mater. 2018, 30, 1707003.
- [42] Y. Wang, Q. Yang, S. Kang, M. A. Wall, J. T. C. Liu, J. Biomed. Opt. 2018, 23, 1.

- [43] S.-A. Yang, S. Choi, S. M. Jeon, J. Yu, Sci. Rep. 2018, 8, 185.
- [44] W. R. Silva, E. L. Keller, R. R. Frontiera, Anal. Chem. 2014, 86, 7782.
- [45] X. Qian, X.-H. Peng, D. O. Ansari, Q. Yin-Goen, G. Z. Chen, D. M. Shin, L. Yang, A. N. Young, M. D. Wang, S. Nie, *Nat. Biotechnol.* 2008, 26, 83.
- [46] G. Q. Wallace, J.-F. Masson, Analyst 2020, 145, 7162.
- [47] D. Kirsch, S. Chen, R. Sidharthan, Y. Chen, S. Yoo, M. Chernysheva, J. Appl. Phys. 2020, 128, 180906.
- [48] T. Itoh, Y. Ozaki, H. Yoshikawa, T. Ihama, H. Masuhara, Appl. Phys. Lett. 2006, 88, 84102.

SUPPORTING INFORMATION

Additional supporting information may be found in the online version of the article at the publisher's website.

How to cite this article: J. E. Olson, J. H. Yu, R. L. Thimes, J. P. Camden, *J. Biophotonics* **2021**, e202100158. https://doi.org/10.1002/jbio.202100158